PCCP

Multichannel Photodissociation Dynamics in CS_2 Studied by Ultrafast Electron Diffraction

Weronika O. Razmus,[a‡] Kyle Acheson,[b‡] Philip Bucksbaum,[c] Martin Centurion,[d] Elio Champenois,[c] Ian Gabalski,[c] Matthias C. Hoffman,[e] Andrew Howard,[c] Ming-Fu Lin,[e] Yusong Liu,[f] Pedro Nunes,[d] Sajib Saha,[d] Xiaozhe Shen,[g] Matthew Ware,[c] Emily M. Warne,[a] Thomas Weinacht,[f] Kyle Wilkin,[d] Jie Yang,[g] Thomas J. A. Wolf,[c] Adam Kirrander,[b,#] Russell S. Minns,[a,*] and Ruaridh Forbes[e,¶]

The structural dynamics of photoexcited gas-phase carbon disulfide (CS_2) molecules are investigated using ultrafast electron diffraction. The dynamics were triggered by excitation of the optically bright $^1B_2(^1\Sigma_u^+)$ state by an ultraviolet femtosecond laser pulse centred at 200 nm. In accordance with previous studies, rapid vibrational motion facilitates a combination of internal conversion and intersystem crossing to lower-lying electronic states. Photodissociation via these electronic manifolds results in the production of CS fragments in the electronic ground state and dissociated singlet and triplet sulphur atoms. The structural dynamics are extracted from the experiment using a trajectory-fitting filtering approach, revealing the main characteristics of the singlet and triplet dissociation pathways. Finally, the effect of the time-resolution on the experimental signal is considered and an outlook to future experiments provided.

1 Introduction

The ultrafast photodissociation dynamics of CS_2 excited by ultraviolet (UV) light have been the subject of wide ranging experimental and theoretical research, with the molecule representing a key target for new ultrafast spectroscopy techniques[1–4]. The apparent structural simplicity of ground state CS_2 belies a complex photochemistry that continues to challenge understanding. The dynamics revolve around rapid structural changes that trigger electronic transitions via competing internal conversion (IC) and intersystem crossing (ISC) processes. The coupled electronic and nuclear dynamics result in cleavage of one of the C-S bonds,

producing electronic ground state CS fragments and singlet or triplet state sulphur atoms,

$$CS_2(X) + h\nu(200\,\text{nm}) \longrightarrow CS(X\,^1\Sigma^+) + \begin{Bmatrix} S(^1D) \\ S(^3P) \end{Bmatrix}. \quad (1)$$
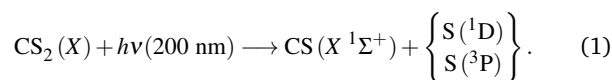
The dissociation occurs on an ultrafast timescale with the spin-forbidden triplet $S(^3P)$ product channel dominating the overall reaction yield[3]. The majority of previous time-resolved studies have focused on the electronic state dynamics, providing only indirect measurements of the structural changes. Here, we report a recent ultrafast electron diffraction (UED) experiment specifically aimed at understanding the structural dynamics at play. A 200 nm pump and a mega-electronvolt (MeV) UED probe are utilised to investigate the nuclear rearrangements following excitation to the $^1B_2(^1\Sigma_u^+)$ electronic state and subsequent photodissociation, occurring via lower-lying manifolds of singlet and triplet states.

Developments in x-ray free electron laser (XFEL)[5] and MeV electron sources[6,7] provide opportunities for accurate measurements of structural dynamics. The ability to combine femtosecond time-resolution with sub-Å spatial resolution means measurements of structural dynamics in electronically excited states of gas phase molecules is now possible[8–13]. The scattering patterns obtained are closely related to the geometry of the molecules and can in principle be transformed to reveal the molecular structure. The challenge lies in the limited momentum transfer range that can be measured, further complicated by effects such as dis-

[a] School of Chemistry, University of Southampton, Highfield, Southampton SO17 1BJ, United Kingdom

[b] EaStCHEM, School of Chemistry and Centre for Science at Extreme Conditions, University of Edinburgh, David Brewster Road, Edinburgh EH9 3FJ, United Kingdom

[c] Stanford PULSE Institute, SLAC National Accelerator Laboratory 2575 Sand Hill Road, Menlo Park, CA 94025, USA

[d] Department of Physics and Astronomy, University of Nebraska–Lincoln, Lincoln, Nebraska 68588, USA

[e] Linac Coherent Light Source, SLAC National Accelerator Laboratory, Menlo Park, California 94025, USA

[f] Department of Physics and Astronomy, Stony Brook University, Stony Brook, New York 11794, USA

[g] SLAC National Accelerator Laboratory, Menlo Park, California 94025, USA

‡ These authors contributed equally to this work

Adam.Kirrander@ed.ac.uk

* R.S.Minns@soton.ac.uk

¶ ruforbes@slac.stanford.edu

persion of the wave packet and branching into different reaction paths which prevent a single representative structure from being meaningfully identified[14]. Extracting accurate structural information therefore often relies on careful comparison to theoretical models and the consideration of multiple structures at any given time delay.

Previous photoelectron spectroscopy measurements of CS_2 exploited molecular alignment and highlighted the rapid internal conversion dynamics linked to the bending and stretching motion in the initially excited $^1B_2(^1\Sigma_u^+)$ electronic state[1,2]. Two more recent extreme ultraviolet (XUV) photoelectron spectroscopy measurements captured the full reaction path from excitation through to product formation[3,4]. Both XUV studies found almost identical time constants and branching ratios for the formation of the two dissociation products.

Quantum beats at the vibrational frequencies associated with the bend and asymmetric stretch in the $^1B_2(^1\Sigma_u^+)$ electronic state were observed in both time-resolved ion yield[15] and UV photoelectron spectroscopy measurements[1,16,17]. The more recent VUV photoelectron imaging[18] and XUV photoelectron spectroscopy work of Suzuki and co-workers[4] achieved impressive temporal resolution that is sufficient to show that these quantum beats are a consequence of large changes in the ionisation potential associated with the bending and stretching geometry changes. The oscillations are subject to rapid damping leading to broad photoelectron signals, indicative of a broad distribution of structures at any one time, and the subsequent dissociation that can be described by simple kinetic equations.
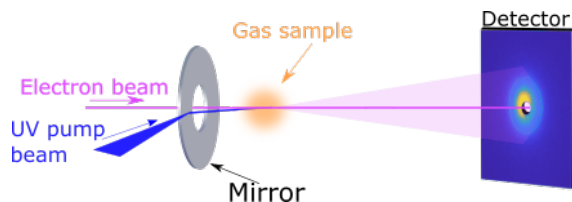

Fig. 1 Schematic of the experimental setup. Free gas-phase CS_2 molecules are excited by a 200 nm (UV) pump pulse, followed by an electron probe pulse in a co-linear geometry, with the scattered electrons recorded on the detector.

In the present study, we provide a complementary structural perspective on the excited state dynamics of CS_2. It is evident that ultrafast diffraction experiments have a high potential to complement ultrafast spectroscopy by resolving the structural motions of the atoms in a molecule undergoing complex photo-excited processes[19,20]. A schematic diagram of the current UED pump-probe experimental setup is shown in Fig. 1. The UED probe tracks the nuclear rearrangements, with the experimental measurements analysed by comparison to calculated diffraction patterns derived from trajectory based dynamics calculations.

The manuscript is structured as follows. In Section 2 descriptions of the experimental setup, analysis methodology and theoretical methods are provided. Section 3 presents the experimental data and provides interpretation of the results via in-depth comparison with theoretical UED results computed on-the-fly from trajectory surface hopping simulations. We also provide an out-

look into the additional information content afforded by future UED experiments should better time resolution be achieved. Finally, our conclusions are summarised in Section 4.

2 Experimental and Theoretical Methods

2.1 Experimental apparatus

The experiment was performed at the SLAC National Accelerator Laboratory using the relativistic MeV-UED beam line. A detailed discussion of the apparatus has been provided in Ref.[7]. Briefly, a Ti:Sapphire laser system ($\lambda = 800$ nm, $\tau \sim 40$ fs pulse duration) is used both to generate the UV pump and the probe electron beam pulses, with pump and probe pulses propagating in near collinear geometry through a gas-cell containing CS_2 molecules. The electron bunch is generated from a photocathode using the third harmonic of the main laser system via standard nonlinear crystal based upconversion techniques. Emitted electron bunches are accelerated to 3.7 MeV in a radiofrequency gun at a repetition rate of 360 Hz. The bunches are focused through an in-vacuum holey mirror to a spot size of 200 μm full-width at half maximum (FWHM) and have an on target pulse duration of approximately 125 fs. The linearly polarized 200 nm pump is produced via a nonlinear crystal based scheme and has pulse duration $\sim$100 fs and an on-target energy of 2 μJ. Separation of the 200 nm light from residual 266 and 800 nm light is achieved using dielectric mirrors from Layertec GmbH. The pulses are focused to a 250 μm (FWHM) diameter spot in the gas cell and recombined with the electron beam at a small angle using the holey mirror. Based on comparison of the static and dynamic signal levels, the excitation fraction is determined to be about 4%. Examination of the relative static and dynamic signal levels as a function of pump laser input intensity also confirmed that the experiments were performed in the linear absorption regime.

The CS_2 sample (Sigma Aldrich, >99%) was used without further purification. Liquid CS_2 was placed in a bubbler and delivered to the gas cell without the use of a seed gas. Control of the sample density and hence signal strength was achieved using a computer-controlled flow controller. The overall path length in the gas cell was $\sim$4 mm. The inner diameter of the cell was 2 mm, with a wall thickness of $\sim$1 mm. A hole diameter of 0.4 mm was used for the current experiments, which prevented sample clogging and facilitated both the laser and electron beams to traverse the cell without clipping. The cell was heated to approximately 100 °C to mitigate sample condensation and cell clogging. For these experiments the *in situ* sample pressure was $\sim$1 Torr, which corresponded to an average collision time of approximately 100 ns (i.e. significantly longer than the current dynamics under investigation).

Scattered electrons from the CS_2 sample were detected using a combination of a phosphor screen and charge coupled device (CCD) camera. The images were accumulated over 20 seconds with 7200 electron bunches (360 Hz) and stored independently allowing for post-processing and/or removal of any bad shots as outlined in Section 2.2. The phosphor screen is equipped with a hole in the center to transmit undiffracted beam electrons, which would otherwise provide very large background signals. CCD im-

ages of the scattered electrons were recorded over one day with multiple time scans added together to form the final data set. Each final diffraction pattern obtained at a particular delay, as reported in the main results section, is the result of combining approximately 185 individual frames.

2.2 Data treatment

The individually measured diffraction patterns were first checked for quality and for any systematic changes in scattering intensity as a function of pump probe delay. The overall scattering intensity in each image was calculated as a simple sum of hits over the full image. Any images with significantly lower scattering intensity (outside of 2 standard deviations of the mean) were removed from further analysis. Systematic changes in scattering intensity with pump-probe delay were also examined but this was found to be stable such that no further action was required. After this quality control step we individually analysed each of the remaining images to identify the centres, given that the image centre can drift or shift due to changes in the electron beam pointing. Variation in the image centre can also occur at high pump laser fluence, when gas molecules can be ionized and turned into plasma. The electric field from the plasma can streak the electron beam and cause diffraction center drift[7]. We intentionally kept the pump-laser power low to reduce the contribution of any plasma such that we expect the pointing stability to be the dominant effect in this experiment. The changes in centre positions were typically small, on the order of a few pixels, but corrections allow for higher resolution to be achieved. The centre of each image was found by applying a least squares fitting algorithm adopted from[21] which finds an average value in a ring at an input radius from an initial guess at the centre position. The algorithm then iteratively improves the guess until it converges on the best-fit centre.

Once centred, the azimuthally averaged diffraction patterns were obtained and combined at each pump-probe delay time. The resulting diffraction patterns were normalised to account for changes in the absolute electron beam bunch charge, estimated at each delay time using the assumption that the total diffracted signal in the momentum transfer range $2 \leq s \leq 8$ Å^{-1} remains constant.

The momentum transfer axis was calibrated using the static CS_2 scattering pattern which was initially converted to $sM(s)$,

$$sM(s) = s \frac{I_{\mathrm{mol}}(s)}{I_{\mathrm{at}}(s)}, \tag{2}$$

where $I_{\mathrm{mol}}(s)$ is the molecular contribution to the total scattering pattern and $I_{\mathrm{at}}(s)$ is the atomic contribution, obtained using form factors[22]. The value of $I_{\mathrm{mol}}(s)$ was obtained from the measured diffraction pattern by subtraction of an initial uniform background and the calculated atomic contribution. The obtained $sM(s)$ was then compared to an independent atom model calculation of $sM(s)$ for CS_2 at its known equilibrium geometry (accounting for the vibrational distribution of geometries in the ground state makes little difference to this process). The comparison allowed us to calibrate from the measured intensity profile in pixels,

to momentum transfer in Å^{-1}. Following calibration the range of momentum transfer measured was $0.95 \leq s \leq 12.25$ Å^{-1}.

To highlight time dependent changes in the data we calculated the percent difference signal as defined by,

$$\%\Delta I_{\mathrm{exp}}(s,t) = 100 \times \frac{I_{\mathrm{exp}}(s,t) - I_{\mathrm{exp}}(s,t \ll 0)}{I_{\mathrm{exp}}(s,t \ll 0)}, \tag{3}$$

where $I_{\mathrm{exp}}(s,t)$ is the normalised total diffraction pattern for each pump-probe delay time t and the reference signal $I_{\mathrm{exp}}(s,t \ll 0)$ is taken to be the average diffraction signal measured at 20 discrete delays -1200 fs $< t < -120$ fs, corresponding to the static, unpumped, CS_2 signal. The advantage of this approach is that it removes static background independent of the excitation, such as the atomic component of the scattering signal, reduces the scaling of the scattering intensity with s, and highlights changes in intensity relative to the ground state equilibrium structure of CS_2. For more information on the decision to perform analysis using $\%\Delta I_{\mathrm{exp}}(s,t)$ rather than the typical $\Delta sM(s,t)$, please refer to Section 1 (specifically subsection 1.3) of the *Supplementary Information*.

The absolute delay stage position of time zero (the delay of maximum overlap between the pump and probe pulses) is not known exactly from analysis of the experimental data alone but was first approximated to within 100 fs by the initial changes seen in the signal. The absolute position of time zero was then more accurately found through comparison of the experimental data to calculated scattering patterns based on trajectory calculations as defined in section 2.3.

The statistical uncertainty in the experimental measurement was calculated using the bootstrapping (jackknifing) method. During the experiment 185 images were collected at each time delay step. For the purposes of the bootstrapping analysis 200 datasets are created by random resampling with replacement, selecting 185 images per delay step 200 times. Each data set is analysed as above such that a mean and standard deviation intensity for each time delay t and momentum transfer s measured can be obtained.

2.3 Extraction of structural dynamics from data

We extract characteristic structural dynamics from the experimental data using a trajectory-fitting approach that filters out the characteristic dynamics in the momentum space, as previously applied to the ring-opening reaction of 1,3-cyclohexadiene[8,19,23,24]. In this approach, the trajectories represent plausible deterministic and continuous reaction paths, which define a sensible molecular space for the inversion. This makes the approach robust with respect to any potential limitations in the experimental data, in particular with respect to limitations in the momentum range detected ($s \in [s_{\min}, s_{\max}]$), but also to aspects such as noise or limited time-resolution. The trajectories are fitted against the experimental data in momentum space, adjusting the weight of each trajectory to achieve the best agreement between the experiment and the resulting model.

In the current treatment, we exploit semiclassical trajectories calculated using the SHARC surface hopping software pack-

age [25–27]. The trajectories start on the optically bright $^1\Sigma_u^+$ state with a total energy corresponding excitation by a ~202 nm pulse and initial coordinates sampled from a ground state Wigner distribution. At time $t = 0$, instantaneous vertical excitation is assumed, which projects the vibrational ground state population onto the excited state. The forces and nonadiabatic couplings are calculated using SA8-CASSCF(10,8)/SVP electronic structure theory [28] and the trajectories are propagated for 1 ps using a 0.5 fs time-step. The 197 trajectories obtained are classified according to their state at the end-time of the simulation as either bound i.e. no dissociation over the duration of the trajectory (48 trajectories), singlet i.e. formation of S(^{1}D) following dissociation of the C−S bond (51 trajectories), or triplet i.e. formation of S(^{3}P) following dissociation of the C−S bond (98 trajectories). Dissociation is defined as occurring at the moment when one of the C−S bonds exceeds 3.4 Å, which is the point of no return in the simulations. Due to instabilities in the electronic structure calculations at large separations, trajectories that dissociate but crash before 1 ps are artificially extended using a combination of a linear extrapolation of the dissociating C-S bond length and a harmonic extrapolation of the remaining CS fragments vibrational motion.

2.3.1 Global optimisation

The weights of the individual trajectories are determined via a least-square fit between predicted and experimental observables as accounted for in the target function. An unbiased search of the parameter space is achieved using a shotgun approach whereby the optimisation is started multiple times from a large set of randomly generated initial values. The global best-fit minimum is selected from the resulting sample of local minima. Each optimisation is performed using a non-linear trust-region reflective algorithm with finite differences [29].

The target function is specified as,

$$F(\mathbf{w},\mathbf{c}) = \sum_i \sum_j p_{\text{conf}}(s_i, t_j + \Delta t) \left| \%\Delta I_{\text{exp}}(s_i, t_j + \Delta t) - \%\Delta I_{\text{th}}(s_i, t_j, \mathbf{w}) \right|^2,$$

(4)

where $\mathbf{w} = (w_1, w_2, \ldots)$ are the normalised trajectory weights, $\|\mathbf{w}\| = 1$, and $\mathbf{c}$ consists of additional factors to be optimised, such as the excitation fraction γ and the time-shift Δt. The confidence matrix, $p_{\text{conf}}(s_i, t_j)$, assigns a weight to each point based on the inverse of the estimated experimental standard deviation, $\sigma(s_i, t_j)$, obtained by the bootstrapping analysis described in section 2.2 (with values renormalised so that maximum confidence corresponds to unity).

The double sum in eqn (4) runs over all experimental data points, identified by the s_i momentum transfer and t_j time coordinates. As mentioned in Section 2.2, the experiment does not directly provide an accurate position for time zero. The experimental data is therefore initially put on an approximate time axis based on an estimate of the position of time zero and a set of preliminary time coordinates. The time-zero is determined by comparison to the theoretical signal using the linear shift Δt in eqn (4). This sets the experimental data on the absolute time axis defined by the pump-probe delay time in the simulations. The percent difference signal for the weighted theory is,

$$\%\Delta I_{\text{th}}(s,t,\mathbf{w}) = 100\gamma \times \frac{I_{\text{th}}(s,t,\mathbf{w}) - I_{\text{ref}}(s)}{I_{\text{ref}}(s)},$$

(5)

where γ is the excitation fraction, $I_{\text{th}}(s,t,\mathbf{w})$ the weighted theory signal, and $I_{\text{ref}}(s)$ the reference signal for the theory. The weighted theory signal is calculated from the trajectories using,

$$I_{\text{th}}(s,t,\mathbf{w}) = \sum_{k=1}^{N_{\text{trj}}} w_k I_k(s,t),$$

(6)

where k is the trajectory index, N_{trj} the number of trajectories, and $I_k(s,t)$ the scattering signal for each trajectory. Currently, we use the rotationally averaged scattering signal obtained with the independent atom model (IAM) and the Debye formula, [30]

$$I_k(s,t) = \sum_{i=1}^{N_{\text{at}}} \sum_{j=1}^{N_{\text{at}}} f_i(s) f_j(s) \frac{\sin\left(sR_{ij}^k(t)\right)}{sR_{ij}^k(t)} + \sum_{i=1}^{N_{\text{at}}} S_{\text{i}}^{\text{inel}(s)},$$

(7)

where the double sum with indices i and j runs over all N_{at} atoms with $f_i(s)$ the corresponding electron scattering form factors [31–33], $R_{ij}^k(t) = |\mathbf{R}_i^k(t) - \mathbf{R}_j^k(t)|$ the internuclear distances between i and j, with the atomic positions $\mathbf{R}_i^k(t)$ taken from the trajectories, and, finally, $S_i^{\text{inel}}(s)$ the inelastic corrections [31]. We note that in the IAM the inelastic scattering is independent of the molecular geometry [34,35] and thus that the inelastic contribution in eqn (7) cancels out in the numerator of the percent difference signal in eqn (5). In contrast, the inelastic contribution remains when calculating the theoretical reference signal, $I_{\text{ref}}(s)$. The $I_{\text{ref}}(s)$, used in eqn (5), is determined using eqn (7) for a set of geometries sampled from the ground state Wigner distribution, taken in practice as the initial ($t = 0$) starting geometries for the ensemble of trajectories.

We now consider the temporal convolution of the theory signal necessary to account for the finite duration of the pump and probe pulses and any temporal jitter.* A Gaussian convolution in the temporal domain is included as,

$$I_k^{\text{conv}}(s,t) = \int_{-\infty}^{\infty} I_k(s,t') \, G(t-t') \, dt'$$

(8)

where the Gaussian point spread function is $G(t) = b_c \exp(-a_c t^2)$ with the normalisation constant $b_c = \sqrt{a_c/\pi}$ and $a_c = 4\ln 2/\tau_c^2$ where τ_c is the FWHM duration of the temporal convolution that accounts for the finite temporal resolution and is identified as the experimental instrument response function (IRF). The temporal convolution of the theory signal also compensates for the instantaneous excitation approximation used in the simulations, and one should therefore note that the temporal convolution is linked to the determination of Δt. The factors γ (excitation fraction), Δt (time-shift) and τ_c (IRF) are determined by scanning the values of Δt and τ_c while optimising γ together with the trajectory weights.
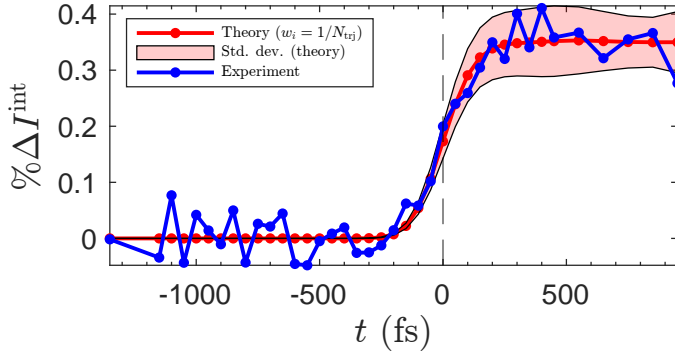
Fig. 2 Fit of the integrated intensity (eqn 9) between 2.8 and 4.2 Å^{-1} from experiment (blue line), with the equally weighted theoretical intensity convolved with a Gaussian of $\tau_c = 230$ fs (FWHM) (red line). Light red shading indicates the standard deviation on the equally weighted theoretical signal. Around time zero, the deviation from the average is small, validating the approximation used in this fit.

2.3.2 Numerical determination of γ, Δt and τ_c

In the first step, we determine the three parameters γ, Δt and τ_c against the strongest and least noisy peak in the experimental signal, a strong peak that raises shortly after $t \approx 0$. The fit is done on the integrated percent difference signal,

$$\%\Delta I^{\text{int}}(t) = \int_{s_0}^{s_1} \%\Delta I(s,t)\, ds, \qquad (9)$$

where the interval $[s_0, s_1] = [2.8, 4.2]\ \text{Å}^{-1}$ contains the peak. Since the theoretical signal for all trajectories is quite similar immediately after $t = 0$, in the first step we use the unbiased theory signal with all trajectories given equal weight, $w_i = 1/N_{\text{trj}}$. The quality of the fit between theory and experiment is scanned for Δt in the range $\Delta t \in [-166, 133]$ fs and for τ_c in the range $\tau_c \in [150, 250]$ fs, the former in steps of 50 fs and the latter in steps of 20 fs. The ranges are chosen based on the known temporal jitter characteristics and duration of the laser and electron pulses. For each pair of Δt and τ_c values, the value of γ is optimised as a free parameter. The experimental data and results for the best fit are plotted in Fig. 2. The optimised values were $\gamma = 3.0\%$, $\Delta t = -83$ fs, and $\tau_c = 230$ fs, and fall well within an experimentally reasonable range, with excitation fractions in line with previous measurements of CS_2, and the temporal response in agreement with previous measurements at the SLAC MeV-UED system. This process places the experimental data on a calibrated and absolute time scale relative to time zero. We note that decreased experimental temporal resolution, relative to the IRF extracted from the laser and electron pulse estimates, is likely due to uncompensated temporal jitter/drifts across the measurement window.

2.3.3 Numerical determination of trajectory weights

The next step is the global optimisation of the trajectory weights $\mathbf{w}$. This is performed with fixed values of Δt and τ_c taken from the previous step but with the excitation fraction γ optimised as a free parameter, the latter providing an independent check on the quality of the two-step procedure. The initial value of γ is taken from step one, while a large set of different initial guesses for the weights $\mathbf{w}$ are generated according to the shotgun procedure. For each initial guess of weights, the optimisation is repeated using the target function in eqn (4), keeping the best fits for the final result.

For a given optimisation, we judge the overall global validity of the fit according to the value of target function, the root mean square deviation (RMSD), and the relative absolute error (RAE). The RMSD between experiment and the optimised theory is defined as,

$$\mu_{\text{RMSD}} = \sum_{s,t} \frac{\sqrt{\left(\%\Delta I_{\text{exp}}(s,t) - \%\Delta I_{\text{th}}(s,t)\right)^2}}{N_{ts} N_s}, \qquad (10)$$

where N_{ts} and N_s refer to the number of points in time and in momentum transfer. Note that in the case of the independent t_0 fit outlined in Section 2.3.2, the average over s is dropped and the RMSD is evaluated on the integrated intensity defined by eqn (9). In addition, we defined the RAE as,

$$\mu_{\text{RAE}} = \sum_{t} \frac{1}{N_{ts}} \frac{\sum_s \frac{1}{N_s} |\%\Delta I_{\text{exp}}(s,t) - \%\Delta I_{\text{th}}(s,t)|}{\sum_s \frac{1}{N_s} |\%\Delta I_{\text{exp}}(s,t) - \%\Delta I_{\text{avg}}(s,t)|}. \qquad (11)$$

Here we normalise the overall RAE by the RAE between the experiment and the unoptimised case corresponding to each trajectory having an equal weight, as given by $\%\Delta I_{\text{avg}}(s,t)$. Hence, a RAE of above 1 means that the optimised fit is worse than equally weighted case, and the lower below 1 means that the optimised result is better.

A further check on the optimisation is that if the re-optimised value of γ deviates significantly from the initial value, this is indicative that the values of Δt and τ_c may not be optimal. Note that the weighting of the diffraction signal with the confidence matrix, $p_c(s_i, t_j')$, is crucial to avoiding over-fitting of noise and achieving a sensible fit.

The best fit yielded a value of $\gamma = 3.4\%$, which deviates from the initial estimate of the excitation fraction by only 0.4%. The small change indicates that the two steps of the optimisation are self-consistent. As a further test of the integrity of the optimisation procedure, we cross-checked that the determination of (γ, t_0, τ_c) in the first step of the optimisation was consistent with the global fit by repeating the process with the second and third best sets of values for $(\gamma, \Delta t, \tau_c)$ from the first step. These sets of values were $(\gamma, \Delta t, \tau_c) = (3.61\%, 16, 230)$ fs and $(3.74\%, 34, 230)$ fs, respectively. More information on the validity of the fits is given in Section 2 of the *Supplementary Information*. It was found that the global optimisation with the *best* initial values from step one consistently resulted in the lowest global RMSD, RAE, *and* the lowest local RMSD around time zero, confirming the consistency of the process.

---

* Note that no convolution of the radial scattering signal with respect to s is necessary as the detector sufficiently resolves the scattering signal.
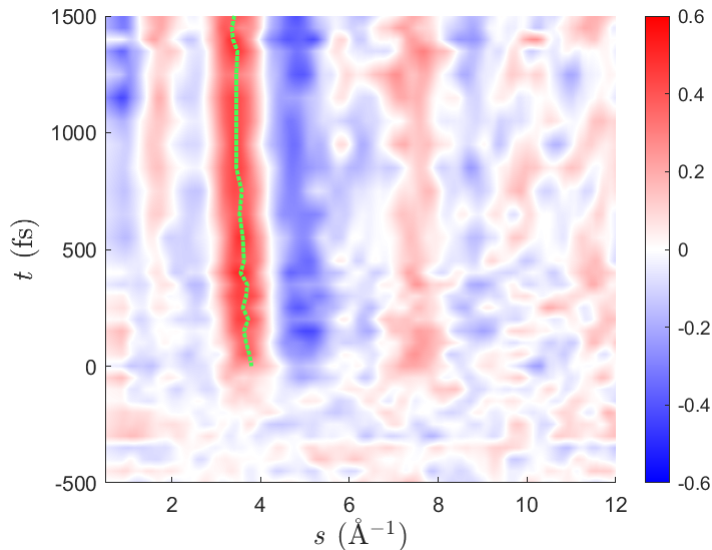
Fig. 3 Colour map of the experimental $\%\Delta I_{\exp}(s,t)$ as a function of the momentum transfer s (Å^{-1}) and pump-probe delay (fs). The dotted green line tracks the center of the first enhancement band at $s \approx 3.8\,\text{Å}^{-1}$, helping to visualise the shift of this band towards lower values of s with increasing pump-probe delay.

3 Results and Discussion

3.1 Experimental signal

We plot the experimentally measured percent difference signal, obtained as set out in Section 2.2, in Figs. 3 and 4. In both figures, positive signals relate to an increase in scattering intensity relative to the ground state, and negative signals to a decrease. Fig. 3 provides an overview of the experimental data across all pump probe delays while in Fig. 4 we plot representative slices through the data at specific pump-probe delays for detailed comparison with theory. At negative pump-probe delays, $t < 0$, when the electron probe precedes the UV pump, the signal is distributed around zero as expected with deviations from zero indicative of noise levels. This is most clearly seen in the $t = -250$ fs slice through the percent difference signal in Fig. 4, where the noise-free theory signal (dotted-blue line) is flat. The observed noise levels are generally higher at high s, commensurate with the s^{-4} scaling of the scattering intensity which means that fewer electrons are detected at high s.

Following excitation at time zero, we observe rapid changes in the difference signal with regions of positive and negative signal across s. The largest changes are observed in the region between 3 and $6\,\text{Å}^{-1}$ with a strong enhancement centred at $s \approx 3.6\,\text{Å}^{-1}$ and a strong depletion at $s \approx 4.7\,\text{Å}^{-1}$. Similar, but weaker, oscillations in the scattering pattern appear at larger values of s, extending all the way out to the edge of the detector. The position of the peaks and troughs in the signal remain fairly stable as the pump-probe delay increases over time but with a broadening and shifting of the positive feature initially centred on $s \approx 3.6\,\text{Å}^{-1}$. This is most clearly seen in Fig. 4 and is also highlighted by a green dashed line that tracks the centre of the peak in Fig. 3. The peak centre undergoes a steady shift from $s \approx 3.79\,\text{Å}^{-1}$ at early times to $s \approx 3.45\,\text{Å}^{-1}$ at $t = 1$ ps, from which point onward the centre re-

mains stationary. The width of the feature also increases from $s \approx 1.4\,\text{Å}^{-1}$ at early times to $s \approx 1.7\,\text{Å}^{-1}$ at $t \approx 1$ ps. Widths are based on the positions at which the peak reaches 50 % of maximum. The timescale of the changes suggests the shift and broadening are indicative of the dissociation process which is known to happen on a similar timescale. In addition, we note another potential indicator of dissociation in the rise in intensity below $2\,\text{Å}^{-1}$. There is a clear delay in the onset of this enhancement, which first appears faintly around the 200 fs mark before steadily rising in intensity with time until is more apparent at around 500 fs. We suggest that this low s feature results from a low frequency contribution to the scattered intensity that describes large separation of the CS and S of the dissociated molecule.
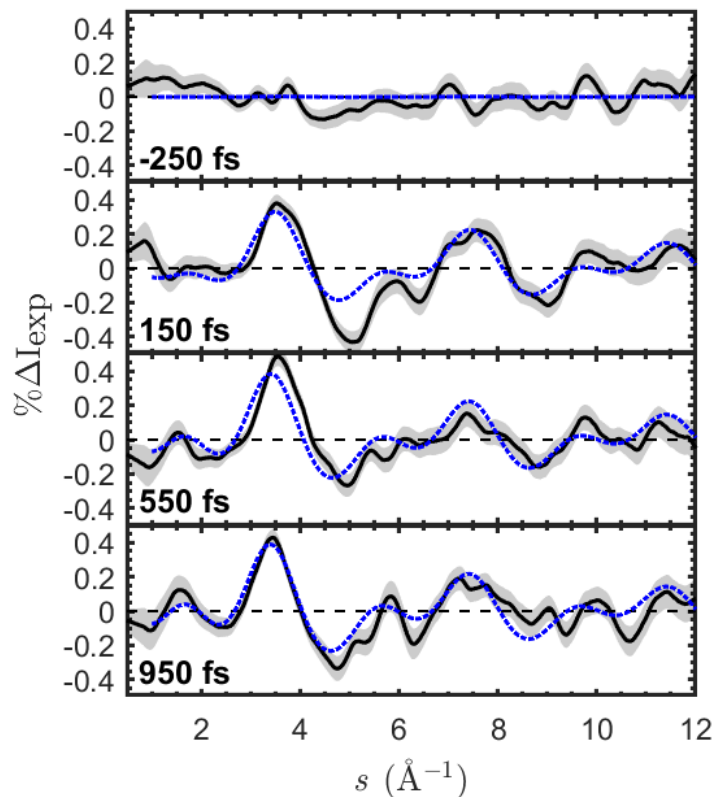

Fig. 4 Percent difference scattering intensity at specific pump-probe delays. Experimental diffraction patterns are plotted as solid black lines with the shaded grey area representing one standard deviation obtained via the bootstrapping analysis. The optimised simulation result is shown as a dotted blue line.

Fig. 4 shows the optimised theory signal resulting from the global fit alongside the experimental data. It is clear that, broadly speaking, the theory provides a good qualitative fit to the experimental signal. Again, the broadening and shifting of the main peak around $3.6\,\text{Å}^{-1}$ is apparent in the theory, capturing the overall structure of the experimental signal but with significantly more shift observed at earlier time compared to the experiment. The optimised theoretical signal results in the peak shifting from around $3.65\,\text{Å}^{-1}$ at t_0 to $3.43\,\text{Å}^{-1}$ at 1 ps. Over all pump-probe delays, the experimental and theoretical shifts observed are in reasonable agreement but with the experimental shifts being slightly larger than those predicted theoretically. The large deple-

tion observed in the experimental data at around $s \approx 4.4\text{-}5$ Å^{-1} at $t = 150$ fs, is not well reproduced but at all other time delays and values of momentum transfer the agreement is quite reasonable (see Fig. S9). A detailed discussion of the validity of the fit is provided in the *Supplementary Information* (Section 2). We now move on to real space analysis of the dynamics, starting with the bond-length pair-distribution function analysis and then moving on to the trajectory analysis.

3.2 Structural dynamics

The structural dynamics are analysed in terms of the trajectories obtained by fitting the experimental signal. We chose to examine the structural dynamics based on the theoretical fits rather than the experimental data for two main reasons. While direct structural information can be obtained via a transform of the experimental data to a change in pair distribution function (ΔPDF), this requires an artificial filling of the low s component due to the hole in the centre of the detector. There are two main approaches that can be applied to "refill" this region, the first is an unbiased extrapolation to zero, while the second utilises calculated data to fill in the gap. We find both approaches to the current data unsatisfactory and given the approach chosen affects the outcome dramatically we have chosen to avoid this step. More details can be found in *Supplementary Information* Section 1.1-1.2 but briefly, linear extrapolation leads to artefacts in the calculated ΔPDF at unphysical distances, while utilising theoretical values unsurprisingly, given the heavy weighting applied to the lower s regions in the damping of the sine transform, leads to Δ PDF's that are heavily biased to the theory input.

The other advantage of using the theoretical values is that while the experiment can provide the ΔPDF, this is a convolution of all geometries measured which would subsequently need to be deconvolved to gain structural insight. The theory can be more readily disentangled to provide details of the underlying dynamics which, through the fitting procedures defined, are consistent with the experimental measurements. We take advantage of this in the next section of the manuscript.

As a first step, a broad overview of the dynamics can be gleaned from the $\Delta \text{PDF}(R,t)$ calculated from the theoretical $\Delta sM(s,t)$ signal. A heat map of the ΔPDF is shown in Fig. 5 (Left), which has four main regions that show time-dependent intensity changes. The two regions that show a net decrease at early times correspond to separations of $1.2 < R < 1.85$ Å (band A) and $2.7 < R < 3.4$ Å (band C), matching the C−S and S−S distances in CS$_2$ at the ground state equilibrium structure (1.55 and 3.1 Å, respectively). The average ΔPDF for regions A and C as a function of time is shown in Fig. 5 (Right), showing the depletion of these characteristic distances as a function of time as the molecular structure evolves. Adjacent to the two regions of reduced intensity, are two regions in which a transient increase in intensity is observed, corresponding to increases in bond length, marked as band B (1.9-2.6 Å) and band D (3.45-4.2 Å) in Fig. 5 (left). The average ΔPDF for bands B and D are also shown in Fig. 5 (Right). The transient increase in these bands is commensurate with bond elongation associated with excited state stretching and bending

dynamics, leading to eventual dissociation. More detail on the dynamics of the system can be obtained from an analysis of the optimised trajectories themselves.

The optimisation yields 8 dominant trajectories with a combined weight of 99.99%, the character of these main trajectories at the end of the simulation, their corresponding weights and their time taken to reach the dissociation point of no return are summarised in table 1. Each of these trajectories should be seen as characteristic representatives of a certain type of dynamics, but are not unique and could be replaced by another, similar trajectory, without overly strong impact on the quality of the fit. The re-weighting of the simulations can therefore be seen as a filtering process that reproduces the experimental signal and distills out the corresponding archetypal dynamics. The effective singlet to triplet ratio according to these trajectories is 1:3.38 with 28% of the population still bound. This compares with the unweighted trajectories which give a branching ratio of 1:1.9 with a remainder bound contribution of 24% at $t = 1$ ps. Both the biased and the unbiased branching ratios are in reasonable agreement with recent time resolved photoelectron spectroscopy measurements[4,36], and those measured in nanosecond experiments measuring the final products[37–43] which provide values around 1:2.5 and 1:3 respectively. The 1:3 ratio from the nanosecond experiments is based on an average of a number of measurements which have provided varied estimates between 4:1 and 1:6. For both the nanosecond and femtosecond measurements it should be noted that these values relate to the asymptotic values rather than the ratio at $t = 1$ ps which, with the dominance of the triplet dissociation channel at longer times, explains the lower values obtained here.

We now analyse the main structural dynamics implied by the fitted trajectories. Fig. 6 shows the C−S distances and associated S−C−S angle for the four most dominant trajectories up to the time of dissociation. The trajectories shown in the two uppermost panels correspond to singlet S(^{1}D) dissociation and the two bottom ones to triplet S(^{3}P) dissociation. Following excitation, the initial vibration is largely symmetric in character with simultaneous bending, but these initial dynamics rapidly couple into more complex motions. Looking at the top set of panels in the figure, showing singlet trajectory 43 (10.35 %), it is evident that the C−S bond dissociates rapidly. In this trajectory, following one cycle of elongation and shortening of the two C−S bonds, the three atoms return to a near-linear arrangement and the momentum is transferred from the more rapidly moving sulphur atom to the opposite sulphur, which is ejected during a sharp bending motion that results in an angle of 111 degrees at the dissociation limit. The remaining CS fragment is left rotating undergoing small-amplitude vibrations. The second, singlet trajectory 90 (4.43 %) shown in the second set of panels from the top, is longer-lived involving low-frequency large amplitude motion of one of the S-atoms, with the molecule exploring a wide range of bond angles. Here, the initial extension of one C−S bond reaches lengths of 2.3 Å, 95% of the way to the dissociation point of no return, within the first few vibrational periods. The S atom, however, remains bound up until 523 fs.

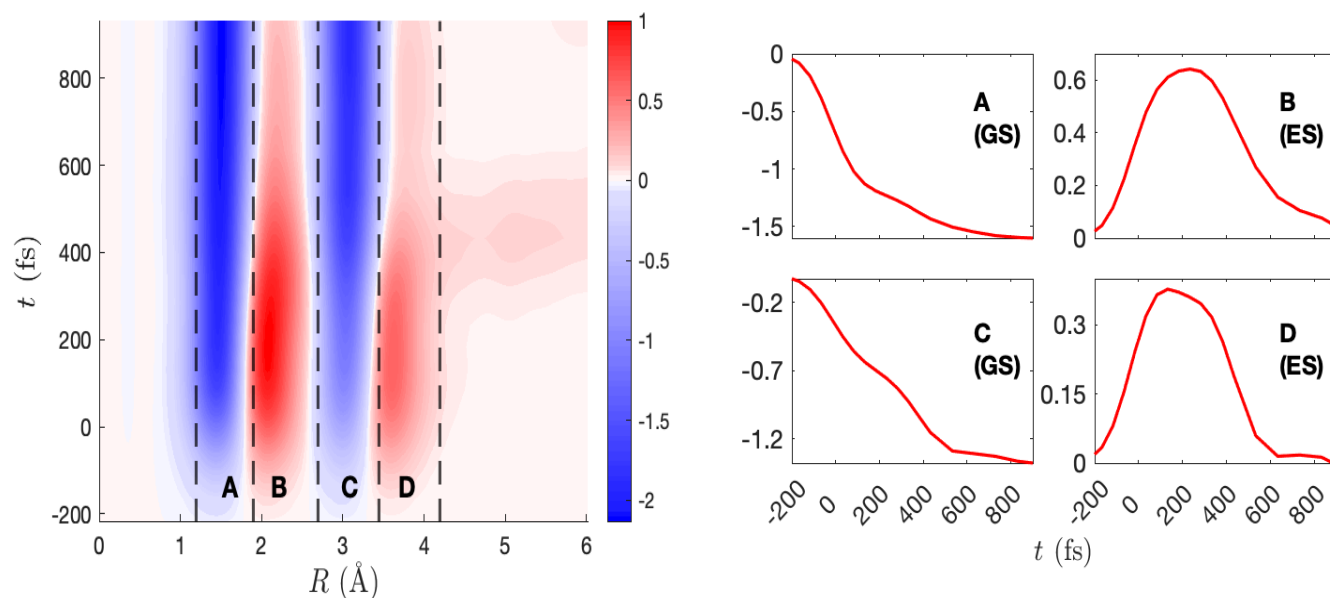Turning to the two triplet trajectories 36 and 176 (44.73 % and

Fig. 5 The left hand side shows the Δ PDF calculated from the theoretical ΔsM. Regions A-D that correspond to the main features are highlighted. On the right hand side one can see the averaged Δ PDF over each of these four regions. Regions A and C are the two depletions, whereas B and D are the two enhancements. These correspond to the ground state (GS) Wigner distribution and the evolution of the nuclear wavepacket upon the excited state (ES) respectively.

7.43 %) shown in the two bottom sets of panels in Fig. 6, we observe that the triplet trajectories show shorter C−S distances on average. The weighted departure velocity of the dissociating sulphur atom is also higher than for the singlets, although this may not be entirely evident from the figure itself. Looking at the early-time motions, it is notable that the triplet trajectories experience stronger initial bending motion, each reaching an angles of 121 and 112 degrees respectively within the first vibrational period. This is an observation which is supported by the simulations where a majority of ISC occurs in strongly bent conformations (see also Ref.[28]).

The optimisation therefore captures the existence of three different classes of dynamics that are defined by their character at the end of the simulations (bound, Singlet, S(^{1}D) production, or Triplet, S(^{3}P) production) and can largely be differentiated based on the time taken to dissociate. Taking each trajectory class in turn, the majority (approx. 63 %) of the singlet signal is comprised of trajectory 43, which has a dissociation time of 132 fs. The remaining singlet contribution comes from trajectories with a longer dissociation time but the lower weighting means this class of trajectories is dominated by a rapid breaking of the CS bond. The dominant triplet contribution (with over 80 % of the total triplet population) corresponds to trajectory 36, which has a dissociation time of 433 fs. The rest of the triplet contribution is from trajectories 96 and 176, each with a dissociation time of 776 and 949 fs, respectively, much longer than any singlet character processes suggesting the triplet states are produced over a much longer time-frame. The remaining contribution to the signal is from the CS$_2$ molecules that remain bound during the time-frame of the measurements. From the fit we can determine the weighted average for the dissociation times of the singlet and triplet classes to be 235 and 523 fs, respectively. The different dissociation times provides a metric for us to differentiate the class of trajectories that are important in the dynamics of the system. While some scattering experiments have shown signatures of differing electronic character of states in some molecular systems[44], we do not see any evidence of this in our measurements and can therefore not directly discern differences in the singlet or triplet character of the final states. Ultimately, we have demonstrated that our procedure captures the rapid singlet dissociation channel through which the majority of the singlet population dissociates, but also the smaller contribution resulting from the slow leakage of the remaining singlet population from longer lived dissociative states. This longer lived singlet dissociation also overlaps with the triplet dissociation channel which while dominant, occurs on slower timescales overall.

Using the theoretical trajectories we can now decompose the time dependent scattering pattern into contributions arising from the three types of trajectory. The decomposition of the scattering signal is plotted in Fig. 7 with contributions from the Singlet (a), Triplet (b) and Bound (c) trajectories separated. A quick visual inspection highlights key differences between the scattering patterns of the dissociative and bound trajectories. The bound trajectories show very minor time dependence after initial excitation with much clearer changes caused by the dissociative trajectories. The dissociative trajectories show clear delayed enhancement just below 2, 6 and 10 Å^{-1} that are absent in the bound contribution to the scattering pattern. The onset of the enhancement correlates well with the calculated dissociation time (dashed black lines in Fig. 7) suggesting that they are signatures of bond dissociation
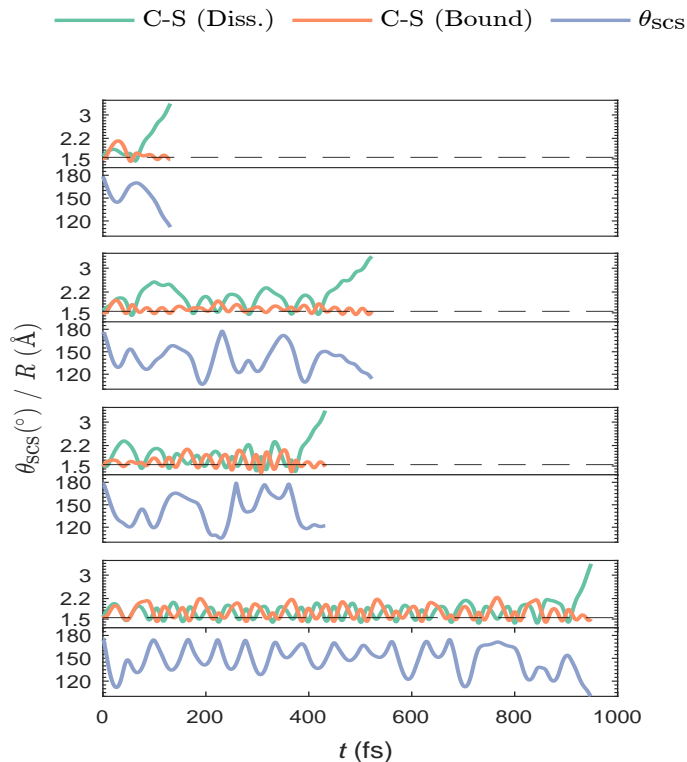
Fig. 6 Atomic C−S distances (Å) and S−C−S bending angles (degrees) in CS$_2$ for the four most significant dissociating trajectories. The dashed black line indicates the ground state equilibrium C−S bond length. The two top sets of panels show the two dominant singlet trajectories, while the two bottom sets of panels show the two dominant triplet trajectories. All trajectories are shown to the point of dissociation.

Fig. 7 Singlet, triplet and bound contributions to the scattering signal calculated from the weighted sum of the optimised trajectories. Black dashed lines represent the dissociation times of the trajectories in table 1.

Trajectory	Weight (%)	Type	Dissociation Time (fs)
14	10.20	Bound	-
36	44.73	Triplet	433
43	10.35	Singlet	132
49	17.81	Bound	-
90	4.43	Singlet	523
93	1.66	Singlet	112
96	3.40	Triplet	776
176	7.43	Triplet	949

Table 1 Summary of the 8 dominant trajectories that result from the best optimisation. These include two bound, three singlet and three triplet trajectories with a total weight of 28 %, 16.45 %, and 55.55 %. Dissociation times are given where applicable.

and extended C-S distances. Commensurate with the increasing intensity is a shift in the main peaks observed in the experiment between 3-6 Å^{-1} indicating this change also correlates with the dissociation dynamics. The peak centred at 3.65 Å^{-1} in theory can also be thought about in terms of its singlet and triplet contributions. The singlet and triplet contributions in Fig. 7 see their main enhancement shift by 0.15 and 0.25 Å^{-1}, respectively. The triplet contribution is expected to exhibit a greater shift due to the fact most dissociation occurs through this channel. This shifting results from a combination of stretching and bending modes, but ultimately the majority of this contribution comes from the asymmetric stretch. The experimental signal in Fig. 3 shows the same structure, where the early rise in intensity below 2 Å^{-1} is due to the S(^{1}D) formation, with the later rise due to a combination of both S(^{3}P) and some minor slower S(^{1}D) formation at longer times. In Fig. S10 one can see there is good agreement with the rise in this intensity between experiment and theory. The separation of trajectories and analysis of the direct scattering patterns allows us to isolate features associated with the structural dynamics that are not immediately obvious from the experimental data alone, or from the ΔPDF shown in Fig. 5.
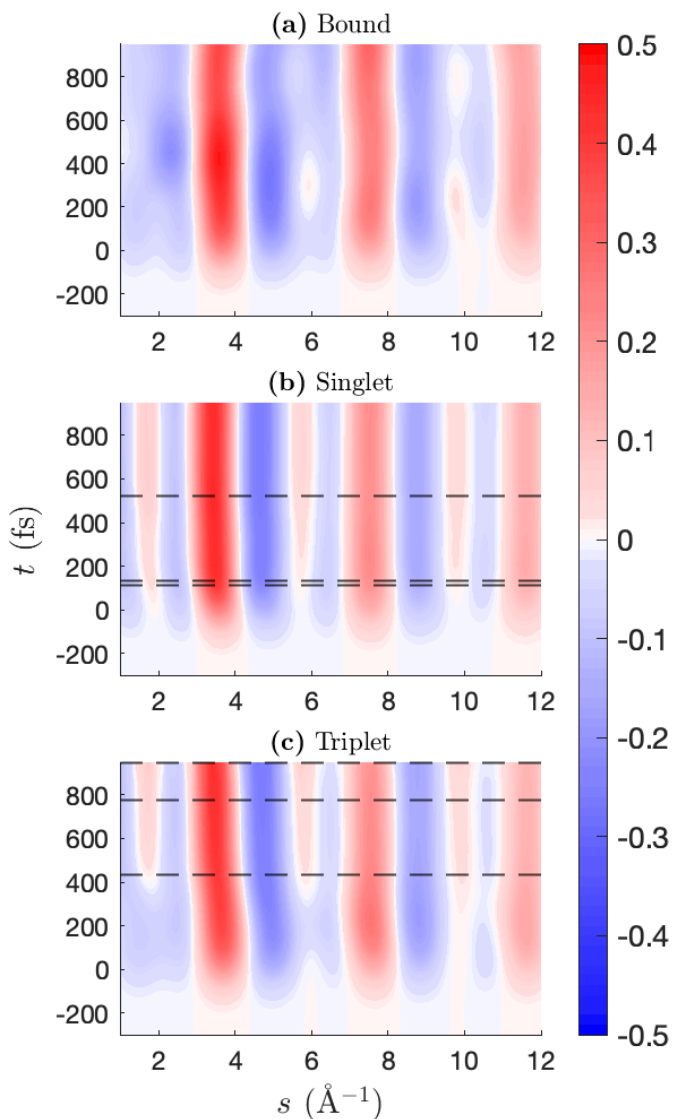
3.3 Observations regarding time-resolution

We conclude the *Results and Discussion* by pointing out that the observation of CS$_2$ photodissociation dynamics would have ben-
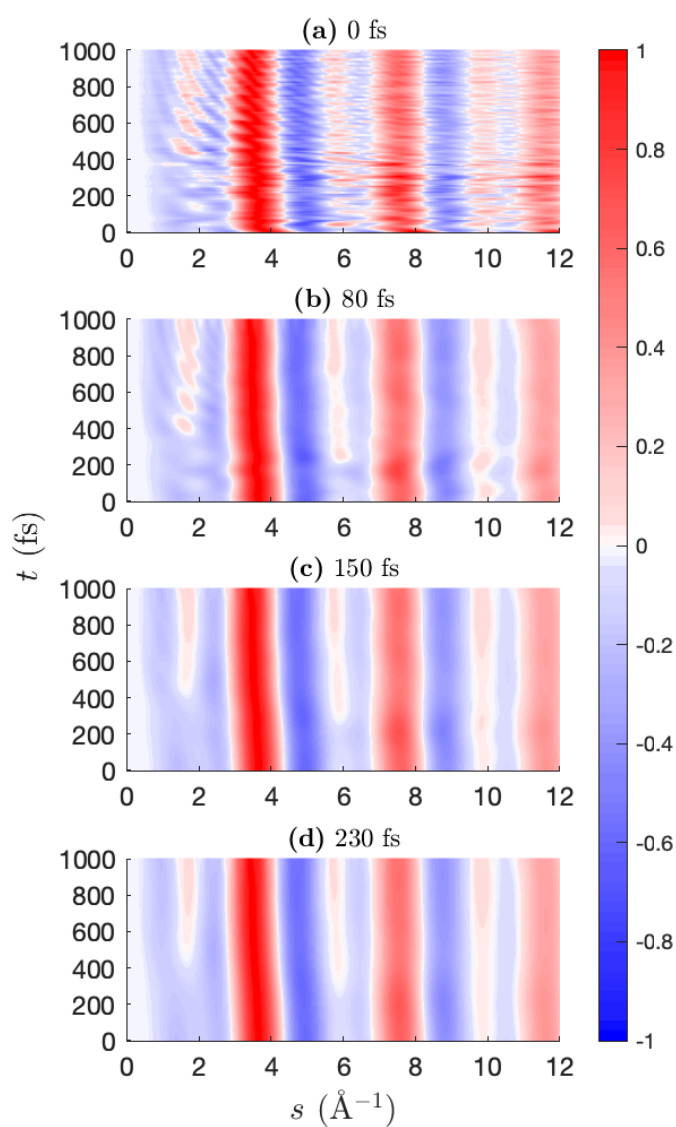
Fig. 8 Plots of the theoretical percentage difference signal $\%\Delta I_{\text{th}}(s,t,\mathbf{w})$ using differing values of the Gaussian width that approximates the IRF. Panels a through d correspond to values of 0, 80, 150, and 230 fs for the IRF respectively. With sub 100 fs temporal resolution, the vibrational fine structure becomes apparent.

efited from better temporal resolution in the experiment. This is illustrated by Fig. 8 which shows the anticipated signal, predicted by the unweighted theory, for values of the IRF ranging from zero to the current 230 fs. It is evident that more detailed features in the signal only become apparent at sub-100 fs temporal resolution, which is unsurprising given that the slowest characteristic vibration in CS_2 is 84 fs. Comparing panels a) and b), corresponding to perfect and 80 fs time-resolution, it is clear that improvements in the time-resolution are necessary to resolve aspects of actual dissociation although the highly disperse nature of the wavepacket and nearly statistical dissociation rate also fundamentally limit the appearance of the dissociation in the experimental diffraction signal. With increased temporal resolution, one could look to exploit the periodicity of different vibrational modes contributions to the main enhancement observed at

3.6 Å^{-1}. As previously touched on, the observed peak shifting is dominated by the asymmetric stretch which occurs on around a 25 fs timescale, this fine structure can be seen in Fig. 8a. However, other slower contributions are present as seen in Fig. 8b, and are the result of bending motion.

4 Conclusions

We have measured and simulated the structural dynamics of the photodissociation of CS_2 following excitation with a 200 nm pulse through the use of ultrafast electron diffraction (UED). The current experiment yields a signal that includes a wide range of the momentum transfer s. Direct interrogation of the experimental signals yields moderate information on the structural dynamics due to competing reaction pathways occurring on similar timescales that mean direct extraction of key structures remains challenging. Coupling the data analysis to a trajectory-fitting strategy based on surface-hopping simulations, however, allows us to infer the characteristic motions coupled to the dissociation. The optimised theory-signal is in good agreement with the scattering signal from the experiment, with an analysis of the various classes of trajectories allowing us to decompose the components of the experimental scattering pattern related to the bound and dissociative trajectories directly. While the ΔPDF is congruent with the dissociation of the molecule, the trajectory-fitting emphasises the greater C−S bond dynamics in the singlet dissociation and the S−C−S bending motions in the triplet dissociation. The trajectory analysis yields sensible values of the excitation fraction, the populations, and branching ratios in accordance with the literature. The rapid dispersion of the wave packet in this system does fundamentally limit how well the structural dynamics can be resolved, something that may also occur in other molecular systems[45]. A second aspect to consider, is that the current conclusions are somewhat limited by the available temporal resolution. With improved time resolution, one could expect a broader range of trajectories selected in the optimisation process, and perhaps more detailed resolution of the dissociation dynamics and lifetimes. Better temporal resolution, combined with improvements in the overall signal levels, would justify more advanced theoretical models beyond IAM to provide the opportunity to unravel electronic effects in the dynamics [13,35,46? ,47].

Conflicts of interest

There are no conflicts to declare.

Acknowledgements

Notes and references

1 C. Z. Bisgaard, O. J. Clarkin, G. Wu, A. M. D. Lee, O. Geßner, C. C. Hayden and A. Stolow, Science, 2009, **323**, 1464–1468.

2 P. Hockett, C. Z. Bisgaard, O. J. Clarkin and A. Stolow, Nat. Phys., 2011, **7**, 612.

3 A. D. Smith, E. M. Warne, D. Bellshaw, D. A. Horke, M. Tudorovskaya, E. Springate, A. J. H. Jones, C. Cacho, R. T. Chapman, A. Kirrander and R. S. Minns, Phys. Rev. Lett., 2018, **120**, 183003.

4 S. Karashima, Y.-I. Suzuki and T. Suzuki, The Journal of Physical Chemistry Letters, 2021, **12**, 3755–3761.

5 P. Emma, R. Akre, J. Arthur, R. Bionta, C. Bostedt, J. Bozek, A. Brachmann, P. Bucksbaum, R. Coffee, F.-J. Decker, Y. Ding, D. Dowell, S. Edstrom, A. Fisher, J. Frisch, S. Gilevich, J. Hastings, G. Hays, P. Hering, Z. Huang, R. Iverson, H. Loos, M. Messerschmidt, A. Miahnahri, S. Moeller, H.-D. Nuhn, G. Pile, D. Ratner, J. Rzepiela, D. Schultz, T. Smith, P. Stefan, H. Tompkins, J. Turner, J. Welch, W. White, J. Wu, G. Yocky and J. Galayda, Nat. Photon., 2010, **4**, 641.

6 S. P. Weathersby, G. Brown, M. Centurion, T. F. Chase, R. Coffee, J. Corbett, J. P. Eichner, J. C. Frisch, A. R. Fry, M. Gühr, N. Hartmann, C. Hast, R. Hettel, R. K. Jobe, E. N. Jongewaard, J. R. Lewandowski, R. K. Li, A. M. Lindenberg, I. Makasyuk, J. E. May, D. McCormick, M. N. Nguyen, A. H. Reid, X. Shen, K. Sokolowski-Tinten, T. Vecchione, S. L. Vetter, J. Wu, J. Yang, H. A. Dürr and X. J. Wang, Rev. Sci. Instrum., 2015, **86**, 073702.

7 X. Shen, J. P. F. Nunes, J. Yang, R. K. Jobe, R. K. Li, M.-F. Lin, B. Moore, M. Niebuhr, S. P. Weathersby, T. J. A. Wolf, C. Yoneda, M. Guehr, M. Centurion and X. J. Wang, Structural Dynamics, 2019, **6**, 054305.

8 M. Minitti, J. Budarz, A. Kirrander, J. Robinson, D. Ratner, T. Lane, D. Zhu, J. Glownia, M. Kozina, H. Lemke, M. Sikorski, Y. Feng, S. Nelson, K. Saita, B. Stankus, T. Northey, J. Hastings and P. Weber, Phys. Rev. Lett., 2015, **114**, 255501.

9 J. Yang, M. Guehr, X. Shen, R. Li, T. Vecchione, R. Coffee, J. Corbett, A. Fry, N. Hartmann, C. Hast, K. Hegazy, K. Jobe, I. Makasyuk, J. Robinson, M. S. Robinson, S. Vetter, S. Weathersby, C. Yoneda, X. Wang and M. Centurion, Phys. Rev. Lett., 2016, **117**, 153002.

10 J. Yang, X. Zhu, T. J. A. Wolf, Z. Li, J. P. F. Nunes, R. Coffee, J. P. Cryan, M. Gühr, K. Hegazy, T. F. Heinz, K. Jobe, R. Li, X. Shen, T. Veccione, S. Weathersby, K. J. Wilkin, C. Yoneda, Q. Zheng, T. J. Martinez, M. Centurion and X. Wang, Science, 2018, **361**, 64–67.

11 T. J. A. Wolf, D. M. Sanchez, J. Yang, R. M. Parrish, J. P. F. Nunes, M. Centurion, R. Coffee, J. P. Cryan, M. Gühr, K. Hegazy, A. Kirrander, R. K. Li, J. Ruddock, X. Shen, T. Vecchione, S. P. Weathersby, P. M. Weber, K. Wilkin, H. Yong, Q. Zheng, X. J. Wang, M. P. Minitti and T. J. Martínez, Nat. Chem., 2019, **11**, 504–509.

12 B. Stankus, H. Yong, N. Zotev, J. M. Ruddock, D. Bellshaw, T. J. Lane, M. Liang, S. Boutet, S. Carbajo, J. S. Robinson, W. Du, N. Goff, Y. Chang, J. E. Koglin, M. P. Minitti, A. Kirrander and P. M. Weber, Nature Chemistry, 2019, **11**, 716–721.

13 H. Yong, X. Xu, J. M. Ruddock, B. Stankus, A. M. Carrascosa, N. Zotev, D. Bellshaw, W. Du, N. Goff, Y. Chang, S. Boutet, S. Carbajo, J. E. Koglin, M. Liang, J. S. Robinson, A. Kirrander, M. P. Minitti and P. M. Weber, Proc. Nat. Acad. Sci., 2021, **118**, e2021714118.

14 A. Kirrander and P. M. Weber, Appl. Science, 2017, **7**, 534.

15 P. Farmanara, V. Stert and W. Radloff, J. Chem. Phys., 1999, **111**, 5338.

16 D. Bellshaw, D. A. Horke, A. D. Smith, H. M. Watts, E. Jager, E. Springate, O. Alexander, C. Cacho, R. T. Chapman, A. Kirrander and R. S. Minns, Chemical Physics Letters, 2017, **683**, 383 – 388.

17 D. Townsend, H. Satzger, T. Ejdrup, A. M. D. Lee, H. Stapelfeldt and A. Stolow, The Journal of Chemical Physics, 2006, **125**, 234302.

18 R. Spesyvtsev, T. Horio, Y.-I. Suzuki and T. Suzuki, The Journal of Chemical Physics, 2015, **142**, 074308.

19 C. C. Pemberton, Y. Zhang, K. Saita, A. Kirrander and P. M. Weber, J. Phys. Chem. A, 2015, **119**, 8832.

20 B. Stankus, J. M. Budarz, A. Kirrander, D. Rogers, J. Robinson, T. J. Lane, D. Ratner, J. Hastings, M. P. Minitti and P. M. Weber, Faraday Discuss., 2016, **194**, 525–536.

21 V. Pratt, SIGGRAPH Comput. Graph., 1987, **21**, 145–152.

22 International Tables for Crystallography Volume C: Mathematical, physical ed. E. Prince, Wiley, 2006th edn, 2006.

23 M. P. Minitti, J. M. Budarz, A. Kirrander, J. Robinson, T. J. Lane, D. Ratner, K. Saita, T. Northey, B. Stankus, V. Cofer-Shabica, J. Hastings and P. M. Weber, Faraday Discuss., 2014, **171**, 81–91.

24 M. Tudorovskaya, R. S. Minns and A. Kirrander, Phys. Chem. Chem. Phys., 2018, **20**, 17714–17726.

25 M. Richter, P. Marquetand, J. González-Vázquez, I. Sola and L. González, J. Chem. Theory Comput., 2011, **7**, 1253–1258.

26 S. Mai, P. Marquetand and L. González, Int. J. Quantum Chem., 2015, **115**, 1215–1231.

27 S. Mai, P. Marquetand and L. González, Wiley Interdiscip. Rev. Comput. Mol. Sci., 2018, **8**, e1370.

28 D. Bellshaw, R. S. Minns and A. Kirrander, Phys. Chem. Chem. Phys., 2019, **21**, 14226–14237.

29 R. H. Byrd, J. C. Gilbert and J. Nocedal, Math. Program., 2000, **89**, 149–185.

30 P. Debye, Ann. Phys., 1915, **351**, 809–823.

31 E. Prince, International Tables for Crystallography Volume C: Mathematical, physical and chemical tables, Springer Netherlands, Dordrecht, 2004.

32 N. F. Mott and W. L. Bragg, Proc. R. Soc., Lond., Ser. A, 1930, **127**, 658–665.

33 H. Bethe, Ann. Phys., 1930, **397**, 325–400.

34 A. M. Carrascosa, H. Yong, D. L. Crittenden, P. M. Weber and A. Kirrander, J. Chem. Theory Comp., 2019, **15**, 2836–2846.

35 N. Zotev, A. M. Carrascosa, M. Simmermacher and A. Kirrander, J. Chem. Theory Comput., 2020, **16**, 2594–2605.

36 E. M. Warne, A. D. Smith, D. A. Horke, E. Springate, A. J. H. Jones, C. Cacho, R. T. Chapman and R. S. Minns, J. Chem. Phys., 2021, **154**, 034302.

37 I. Waller and J. Hepburn, J. Chem. Phys., 1987, **87**, 3261–3268.

38 W.-B. Tzeng, H.-M. Yin, W.-Y. Leung, J.-Y. Luo, S. Nourbakhsh, G. Flesch and C. Ng, J. Chem. Phys., 1988, **88**, 1658–1669.

39 W. S. McGivern, O. Sorkhabi, A. H. Rizvi, A. G. Suits and S. W. North, J. Chem. Phys., 2000, **112**, 5301–5307.

40 T. N. Kitsopoulos, C. R. Gebhardt and T. P. Rakitzis, J. Chem. Phys., 2001, **115**, 9727–9732.

41 S. Yang, A. Freedman, M. Kawasaki and R. Bersohn, J. Chem. Phys., 1980, **72**, 4058–4062.

42 M. Addison, R. Donovan and C. Fotakis, Chem. Phys. Lett., 1980, **74**, 58–62.

43 V. McCrary, R. Lu, D. Zakheim, J. Russell, J. Halpern and W. Jackson, J. Chem. Phys., 1985, **83**, 3481–3490.

44 J. Yang, X. Zhu, J. P. F. Nunes, J. K. Yu, R. M. Parrish, T. J. A. Wolf, M. Centurion, M. Gühr, R. Li, Y. Liu, B. Moore, M. Niebuhr, S. Park, X. Shen, S. Weathersby, T. Weinacht, T. J. Martinez and X. Wang, Science, 2020, **368**, 885–889.

45 V. Makhija, A. E. Boguslavskiy, R. Forbes, K. Veyrinas, I. Wilkinson, R. Lausten, M. S. Schuurman, E. R. Grant and A. Stolow, Faraday Disc., 2021, **228**, 191–225.

46 T. Northey, N. Zotev and A. Kirrander, J. Chem. Theory Comput., 2014, **10**, 4911.

47 T. Northey, A. M. Carrascosa, S. Schäfer and A. Kirrander, J. Chem. Phys., 2016, **145**, 154304.